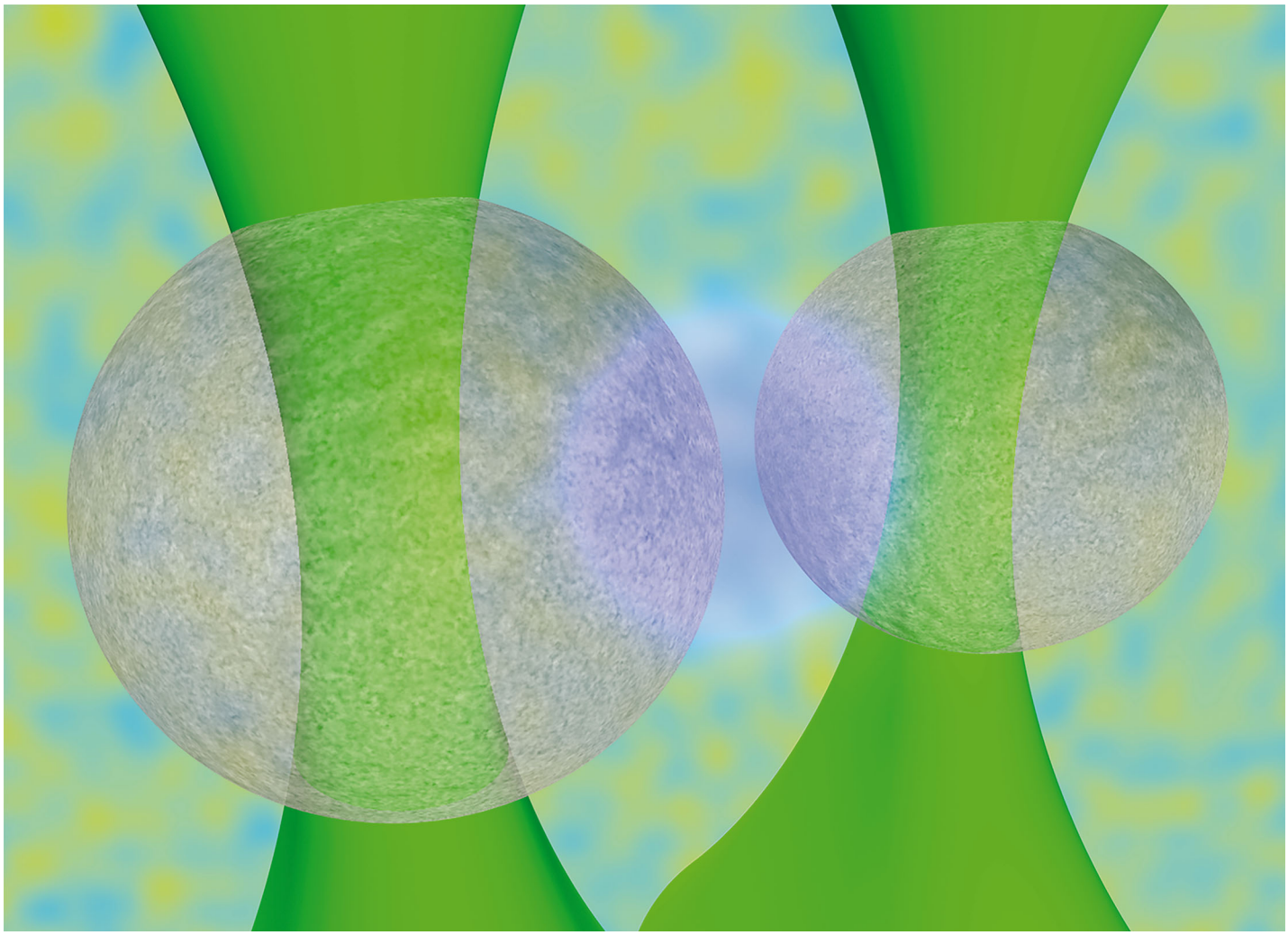

Highlighting research from the Soft Matter Lab from the group of Dr Giovanni Volpe.

Controlling the dynamics of colloidal particles by critical Casimir forces

Critical Casimir forces can affect the dynamics of colloidal particles as a function of the temperature and of the surface properties of the involved objects. Magazzù *et al*. put forward new possibilities for the design and realization of self-assembled nanostructures and for driving nanodevices.

As featured in:

See Alessandro Magazzù *et al*., *Soft Matter*, 2019, **15**, 2152.

ROYAL SOCIETY OF CHEMISTRY | Celebrating IYPT 2019

rsc.li/soft-matter-journal

Registered charity number: 207890

Soft Matter

PAPER

View Article Online
View Journal | View Issue

Cite this: *Soft Matter*, 2019, **15**, 2152

Controlling the dynamics of colloidal particles by critical Casimir forces

Alessandro Magazzù, *[a] Agnese Callegari, [b] Juan Pablo Staforelli, [c] Andrea Gambassi, [d] Siegfried Dietrich[ef] and Giovanni Volpe [ab]

Received 5th July 2018,
Accepted 10th January 2019

DOI: 10.1039/c8sm01376d

rsc.li/soft-matter-journal

Critical Casimir forces can play an important role for applications in nano-science and nano-technology, owing to their piconewton strength, nanometric action range, fine tunability as a function of temperature, and exquisite dependence on the surface properties of the involved objects. Here, we investigate the effects of critical Casimir forces on the free dynamics of a pair of colloidal particles dispersed in the bulk of a near-critical binary liquid solvent, using blinking optical tweezers. In particular, we measure the time evolution of the distance between the two colloids to determine their relative diffusion and drift velocity. Furthermore, we show how critical Casimir forces change the dynamic properties of this two-colloid system by studying the temperature dependence of the distribution of the so-called first-passage time, *i.e.*, of the time necessary for the particles to reach for the first time a certain separation, starting from an initially assigned one. These data are in good agreement with theoretical results obtained from Monte Carlo simulations and Langevin dynamics.

1 Introduction

Critical Casimir forces (CCFs) arise in a binary liquid mixture close to its critical point.[1–5] Upon approaching the critical point, fluctuations of the composition of the mixture emerge. If these critical fluctuations are confined between neighboring objects (*e.g.*, two colloids, or a colloid and a planar surface), they lead to effective forces between these objects. These so-called CCFs were first predicted theoretically in 1978 by M. E. Fisher and P. G. de Gennes[1] in analogy to quantum-electrodynamical (QED) Casimir forces.[6] Only recently have they been measured directly[7–9] and proved to be relevant for soft matter.[10–12] These CCFs have been enjoying significant interest both from basic research and because they are promising candidates for applications in nano-science and nano-technology, in order to manipulate objects (*e.g.*, by controllable periodic deformations of chains), to assemble devices (*e.g.*, *via* the self-assembly of colloidal molecules[13,14]), and to drive machines (*e.g.*, by powering rotators[15]) at the nano- and micro-meter scale. In fact, their piconewton strength and nanometric ranges of action match the requirements of nano-technology. Furthermore, these forces show an exquisite dependence on the temperature of the environment and on the chemical surface properties of the objects involved.[4,5,8,16,17] For example, if composition fluctuations are confined between particles with the same surface property (*e.g.*, hydrophilic), attractive CCFs take hold, while they are repulsive between particles with opposite surface properties (*e.g.*, hydrophilic *vs.* hydrophobic particles). With the exception of ref. 18, until now, the experimental studies have focused on the time-independent properties of CCFs and thus keeping their dynamics hidden. Here, we use blinking optical tweezers to reveal how CCFs affect the free dynamics of a pair of colloidal particles immersed in a binary solution.

2 Experimental setup and methods

In our experiment, we use silica microspheres with diameter $d = 2.06 \pm 0.05$ μm (Microparticles GmbH), dispersed in a critical mixture of water and 2,6-lutidine at the critical lutidine mass fraction $c_L^c = 0.286$, corresponding to a lower critical point at the temperature $T_c \simeq 34$ °C.[19,20] In the bulk of the critical mixture, we generate two holographic optical traps[21,22] at positions $\mathbf{R}_{0,1}$ and $\mathbf{R}_{0,2}$ in order to fix the positions $\mathbf{R}_1$ and $\mathbf{R}_2$ of the centers of two spherical colloids at their initial values, approximately equal to $\mathbf{R}_{0,1}$ and $\mathbf{R}_{0,2}$, respectively, with a specified center-to-center distance $r_0 = 2.40$ μm (Fig. 1a). We have chosen this value for r_0 such that the resulting surface-to-surface distance between the two colloids is of the order of

[a] *Department of Physics, University of Gothenburg, SE-41296 Gothenburg, Sweden. E-mail: alessandro.magazzu@physics.gu.se*
[b] *Soft Matter Lab, Department of Physics and UNAM – National Nanotechnology Research Center, Bilkent University, Ankara 06800, Turkey*
[c] *Department of Physics, University of Concepción, 160-C, Concepción, Chile*
[d] *SISSA – International School for Advanced Studies and INFN, 34136 Trieste, Italy*
[e] *Max Planck Institute for Intelligent Systems, 70569 Stuttgart, Germany*
[f] *IVth Institute for Theoretical Physics, University of Stuttgart, 70569 Stuttgart, Germany*

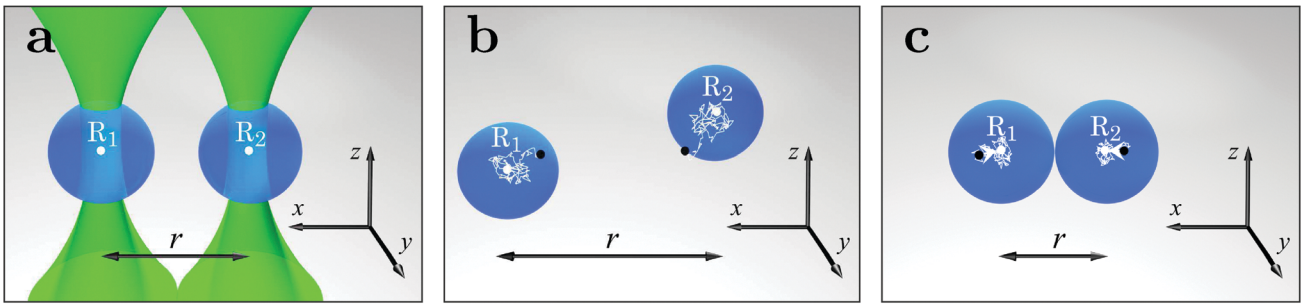

Fig. 1 Schematic presentation of the design of the experiment. (a) Two equal spherical silica colloids (blue spheres, diameter d = 2.06 ± 0.05 μm) are optically trapped by two traps (green laser beams focused on the points $\mathbf{R}_{0,1}$ and $\mathbf{R}_{0,2}$) in the bulk of a binary liquid mixture of water and 2,6-lutidine. The centers of the two colloids shown in the figure are located at positions $\mathbf{R}_{1,2}$ (rather close to $\mathbf{R}_{0,1}$ and $\mathbf{R}_{0,2}$), and the lateral distance between them, *i.e.*, projected onto the *xy*-plane which the laser beams are orthogonal to, is indicated by the black arrowed line r. (b) If the temperature of the mixture T is sufficiently far away from the critical temperature T_c (*i.e.*, $T_c - T = \Delta T \gtrsim 500$ mK), upon switching off the optical tweezers by blocking the laser beam, the two colloids start to diffuse freely in the solvent. The positions of the colloids change from their initial values $\approx \mathbf{R}_{0,1}$ and $\approx \mathbf{R}_{0,2}$, indicated by the black dots, to the final ones $\boldsymbol{R}_1$ and $\boldsymbol{R}_2$, respectively, indicated by the white dots, following the irregular white trajectory. (c) As T approaches T_c, attractive CCFs (white arrows) arise and affect the dynamics of the particles such that there is a large probability for them to approach each other.

300 nm. Accordingly, the latter is significantly larger than the range of the electrostatic repulsion (which holds up to a surface-to-surface distance of about 100 nm, because the Debye screening length is $\ell_D \simeq 13$ nm[9,20]) and comparable with the largest range of the CCFs achieved in the present experiment (which here are always negligible beyond ≈300 nm). Given the sensitivity of CCFs to temperature, the sample temperature is stabilized to within ±2 mK[9] *via* a feedback controller, through the microscope objective. Although the objective is the closest metallic element to the trapping region, the actual temperature of the liquid mixture may differ slightly from the one measured at the objective. The values of the temperature reported in this paper are those of the mixture, which we infer *a posteriori* from the data analysis according to the method discussed in detail in ref. 9. The scheme of the experimental setup is presented in Fig. 2.

We periodically chop the laser beam at the blinking frequency f_b = 1.3 Hz so that the optical traps are periodically switched on and off (blinking optical tweezers[23–25]). We have chosen this value of f_b because it is sufficiently low in order to be able to observe the effects of CCFs on the particle dynamics in the *xy*-plane and high enough to permit us to neglect the effects of gravity on the vertical position z of the particle. We record the ensuing motion of the colloids at 300 fps during the time windows in which the beam is blocked and hence the optical potential is not present. When the traps are turned on again, the two colloids are brought back to their initial positions by the restoring forces of the optical potentials. If the temperature T of the mixture is sufficiently far from T_c (*i.e.*, $\Delta T = T_c - T \gtrsim 500$ mK), the two particles freely diffuse in the solution as long as the optical traps are off (Fig. 1b). When $\Delta T \to 0$, critical order parameter fluctuations take hold associated with an increasing correlation length ξ. As ξ becomes comparable to the inter-particle distance r, the two hydrophilic particles experience attractive CCFs, which affect their dynamics and reduce their inter-particle distance (Fig. 1c). The entire blinking process is repeated about 400 times for each fixed value of $\Delta T \to 0$ in order to acquire sufficient statistics for the dynamics of the colloids.

We have analyzed the acquired videos using digital video microscopy[22,26] in order to determine the trajectories $\mathbf{r}_1(t)$ and $\mathbf{r}_2(t)$ of the centers of the two particles projected onto the *xy*-plane, where $\mathbf{r}_l(t) = (x_l(t), y_l(t))$ with l = 1,2 labelling the particles. We correct the relative position of the particles $\mathbf{r}(t) = \mathbf{r}_2(t) - \mathbf{r}_1(t)$ and their relative distance $r(t) = |\mathbf{r}(t)|$ to account for artefacts which appear in digital video microscopy due to the proximity between the two particles.[9,27]

3 Data analysis and results

3.1 Particle trajectories and time evolution of the inter-particle distance probability density

In Fig. 3 several inter-particle projected distances $r(t)$ are reported for decreasing values of ΔT. For each value of ΔT, we plot the evolution of the inter-particle distance probability density as a function of time obtained from 400 particle trajectories by binning (colored background). We highlight a few selected trajectories to illustrate typical behaviors of the particles (solid lines). For ΔT = 456 ± 2 mK (Fig. 3a), the particles are diffusing freely and the CCFs do not affect their behavior. Heuristically, this is suggested by the fact that the probability density of the inter-particle distance is rather broad compared to what is observed closer to criticality. More quantitatively, the absence of CCFs is proved by the analysis presented further below. When ΔT is reduced to ΔT = 200 ± 2 mK (Fig. 3b) and 163 ± 2 mK (Fig. 3c), the CCFs arise and affect the dynamics of the colloids. Occasionally they cause adhesion as can be inferred from the emergence of a peak in the inter-particle distance probability density at $r \approx 2.16$ μm. If ΔT is reduced further to ΔT = 108 ± 2 mK (Fig. 3d), strong attractive CCFs hinder the free diffusion of the particles, which often adhere to each other so that the values of r lie within a small region in which there is a balance between the repulsive electrostatic forces and the attractive CCFs.

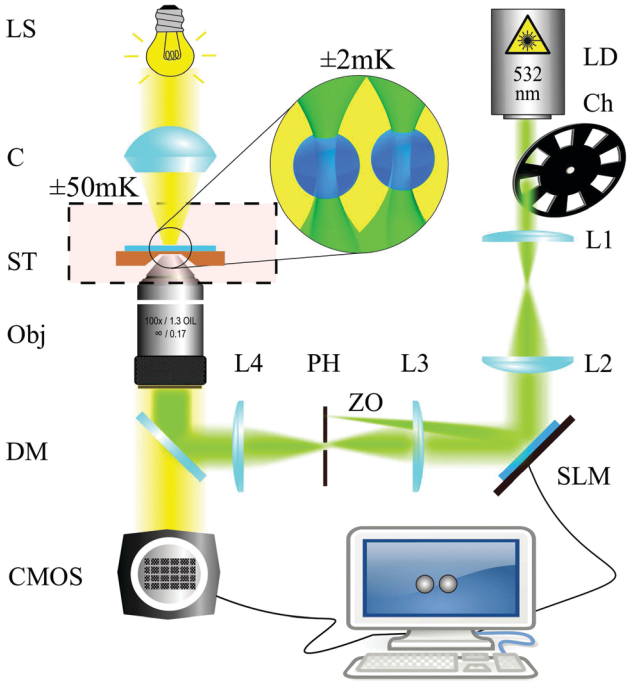

Fig. 2 Scheme of the experimental setup. The experimental setup consists of three main parts: holographic optical tweezers, a digital video microscope, and a temperature control unit. The holographic optical tweezers generate two optical traps by imposing a phase-only hologram on an incoming laser beam *via* a spatial light modulator (SLM) and by focusing the resulting beam through an oil-immersion objective (Obj) (with magnification 100× and numerical aperture NA = 1.30). The laser beam with a wavelength of 532 nm is generated by a laser diode (LD) and the traps are periodically switched on and off by a chopper (Ch). A telescope consisting of two lenses (L1 and L2) is used to overfill the active area of the SLM. Two other lenses (L3 and L4) and a pinhole (PH) are used for blocking the zeroth order (ZO) of the reflected beam. The digital video microscope is used to track the positions of the colloidal particles by illuminating the sample with a white light source (LS), focused by a condenser (C). A dichroic mirror (DM) is used to combine the optical paths of the laser and of the white light. The entire trapping process is imaged by a CMOS camera. The temperature of the whole sample stage (ST) is stabilised with a precision of 50 mK. It is located inside an enclosed chamber indicated by the shaded, pink area with a dashed contour. The temperature of the focal region (inset) is stabilised to within ±2 mK through the microscope objective with a feedback controller.

3.2 Equilibrium distributions and parameter fitting

At a specific temperature ΔT, the initial values $\mathbf{r}_{1,2}(0)$ of the recorded trajectories are sampled from the equilibrium distribution of the two trapped particles exposed to the optical potentials $V_{\mathrm{ot},1}(\mathbf{R}_1) + V_{\mathrm{ot},2}(\mathbf{R}_2)$, to the electrostatic repulsion $V_{\mathrm{es}}(\rho)$, and possibly to CCFs $V_{\mathrm{C}}(\rho)$, *i.e.*, to the total potential

$$V(\mathbf{R}_1,\mathbf{R}_2) = V_{\mathrm{ot},1}(\mathbf{R}_1) + V_{\mathrm{ot},2}(\mathbf{R}_2) + V_{\mathrm{es}}(\rho) + V_{\mathrm{C}}(\rho), \qquad (1)$$

where $\rho = |\mathbf{R}_2 - \mathbf{R}_1| - d$ is the actual surface-to-surface distance between the two colloids, and $\mathbf{R}_l = (x_l,y_l,z_l)$ with $l = 1, 2$ are their initial positions. Note that the projected distance r introduced above is generically smaller than the actual center-to-center distance $|\mathbf{R}_2 - \mathbf{R}_1|$, due to possible displacements of the colloids along the vertical z direction. The optical potentials $V_{\mathrm{ot},1}$ and $V_{\mathrm{ot},2}$ reported in eqn (1) are assumed to be harmonic, *i.e.*,

$$V_{\mathrm{ot},l}(\mathbf{R}_l) = \frac{1}{2}k_l(\mathbf{R}_l - \mathbf{R}_{0,l})^2, \qquad (2)$$

where the center $\mathbf{R}_{0,l}$ of trap $l = 1, 2$ and the stiffnesses $k_{1,2}$ are determined experimentally by the calibration of the two optical traps separately, as described in ref. 9. These values are then used and fixed in all the subsequent analyses.

For the electrostatic repulsion potential V_{es}, we consider the simple expression[9,20]

$$V_{\mathrm{es}}(\rho) = k_{\mathrm{B}}T_{\mathrm{c}}\, \mathrm{e}^{-(\rho-\rho_{\mathrm{es}})/\ell_{\mathrm{D}}}, \qquad (3)$$

where ρ is the surface-to-surface distance between the colloids, ρ_{es} is an effective parameter, which depends on the surface charges, while ℓ_{D} is the Debye screening length.[9,20]

For the potential V_{C} of the CCFs, we adopt the theoretical prediction

$$V_{\mathrm{C}}(\rho) = k_{\mathrm{B}}T_{\mathrm{c}}\frac{d}{4\rho}\Theta(\rho/\xi), \qquad (4)$$

based on the Derjaguin approximation (see, *e.g.*, ref. 20). Θ is a universal scaling function, inferred from the numerical estimates available in the literature,[9,28–30] and ξ is the bulk correlation length of the critical fluctuation of the order parameter of the binary liquid mixture. During the time windows when the optical traps are switched on, the positions of the particles evolve under the action of the total potential $V(\mathbf{R}_1,\mathbf{R}_2)$, and, after a sufficiently long time, they reach the equilibrium distribution $P_{\mathrm{eq}}(\mathbf{R}_1,\mathbf{R}_2) \propto \exp[-V(\mathbf{R}_1,\mathbf{R}_2)/(k_{\mathrm{B}}T)]$. Accordingly, when the optical traps are switched off, the distribution of the initial positions of the particles renders $P_{\mathrm{eq}}(r)$, which follows from $P_{\mathrm{eq}}(\mathbf{R}_1,\mathbf{R}_2)$ by integrating over all the possible configurations with projected center-to-center distance equal to r, *i.e.*, $P_{\mathrm{eq}}(r) = \int \mathrm{d}^3\mathbf{R}_1\mathrm{d}^3\mathbf{R}_2 P_{\mathrm{eq}}(\mathbf{R}_1,\mathbf{R}_2)\delta(r - |\mathbf{r}_1 - \mathbf{r}_2|)$, where we remind that $\mathbf{r}_l$ is the projection of $\mathbf{R}_l$ onto the xy-plane. These distributions are reported in Fig. 4 for the same values of ΔT as considered in Fig. 3. The histograms represent the experimentally measured data, and the solid lines are the corresponding theoretical results obtained from the Monte Carlo integration of $P_{\mathrm{eq}}(\mathbf{R}_1,\mathbf{R}_2)$, introduced above.

For $\Delta T = 456 \pm 2$ mK (Fig. 4a), $P_{\mathrm{eq}}(r)$ can be very well approximated by a Gaussian distribution centered at the value $r \simeq 2.40$ μm, corresponding to the distance r_0 between the minima of the two optical potentials. This result is expected for two optically trapped particles which do not interact with each other.[22] Reducing ΔT (Fig. 4b–d), a peak arises at $r \simeq 2.16$ μm on the left flank of the Gaussian distribution, becoming more dominant at the expense of the Gaussian distribution. This is due to the gradual emergence of attractive CCFs between the particles, which causes them to adhere to each other also in the presence of the optical potentials. The peak position indicates the region where the repulsive electrostatic forces and the attractive CCFs are balanced.

By using Monte Carlo integration, we also calculated the distribution $P_{\mathrm{eq}}(r)$ on the basis of the theoretical potential

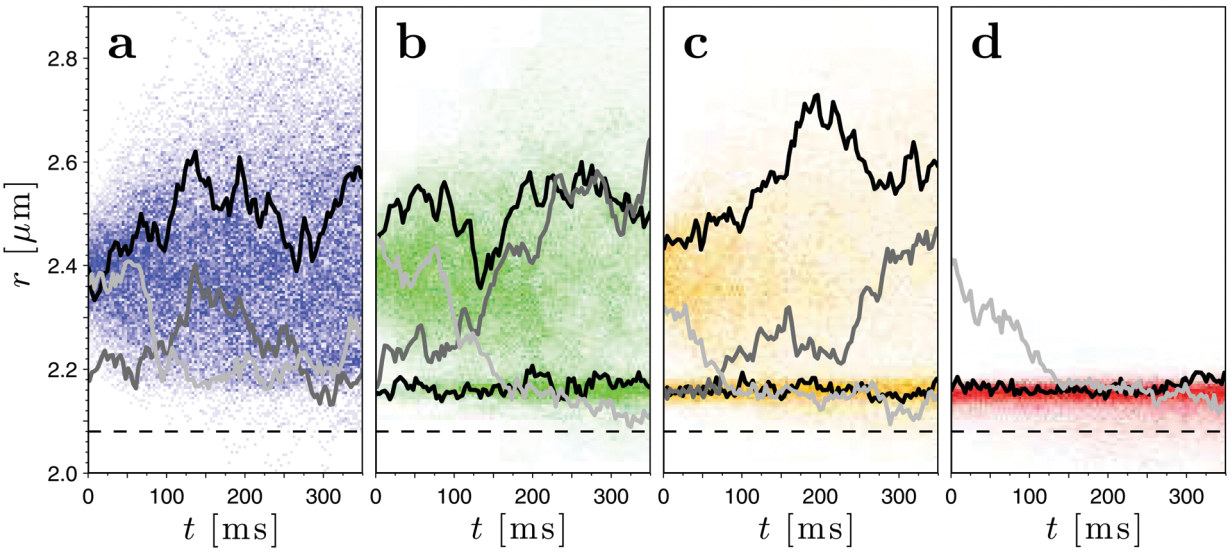

Fig. 3 Time evolution of the projected inter-particle distances $r(t)$ after the optical tweezers are switched off at $t = 0$ for decreasing values of ΔT: (a) $\Delta T = 456 \pm 2$ mK, (b) 200 ± 2 mK, (c) 163 ± 2 mK, and (d) 108 ± 2 mK. The solid lines indicate representative individual trajectories while the intensities of the background colors represent the evolution of the particle position probability distribution obtained from 400 different trajectories. From (a to d), the free diffusion of the colloids is increasingly affected by the emergence of attractive CCFs upon approaching criticality. The dashed horizontal line indicates the projected inter-particle distance r corresponding to the diameter d of the colloids. Sometimes $r(t)$ is smaller than d because a displacement of the colloids along the vertical z-axis causes their projections onto the xy-plane to overlap. This occurs more frequently in the presence of CCFs and particularly if the particles are stuck together. These cases, however, are rare compared to those in which the particles do not leave the xy-plane.

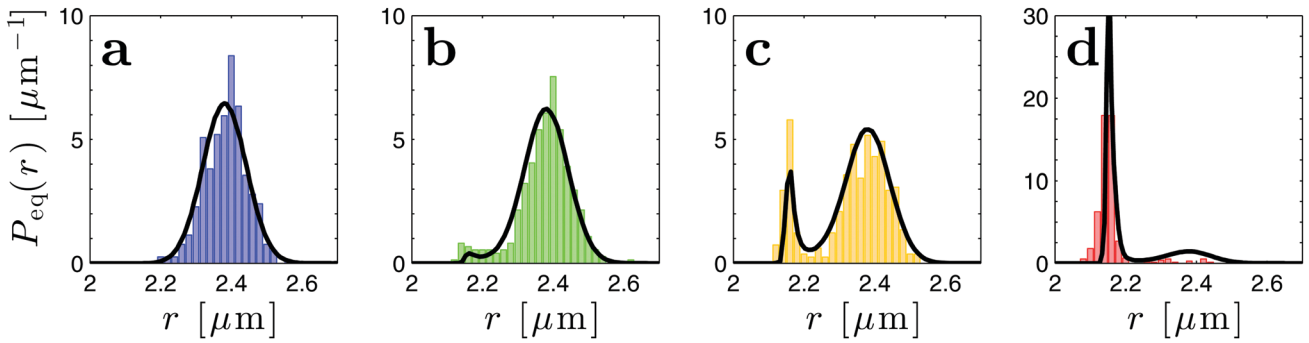

Fig. 4 Equilibrium distribution $P_{eq}(r)$ of the inter-particle distance $r(0)$ (*i.e.*, when the optical tweezers are switched off) for two optically trapped colloids at temperatures (a) $\Delta T = 456 \pm 2$ mK, (b) 200 ± 2 mK, (c) 163 ± 2 mK, and (d) 108 ± 2 mK. Each histogram is obtained from 400 different experimental values. The solid black lines are the theoretical distribution of $r(0)$, obtained *via* Monte Carlo integration (10^6 samples) of two optically trapped particles subjected to the theoretical total potential $V(\mathbf{R}_1,\mathbf{R}_2)$ (eqn (1)).

$V(\mathbf{R}_1,\mathbf{R}_2)$. In particular, we have used $V_{ot,l}(\mathbf{R}_l)$ (eqn (2)) and $\Theta(\rho/\xi)$ (eqn (4)) as input functions and ρ_{es}, ℓ_D, and ξ as fitting parameters. It is worth noting that the fitting parameters ρ_{es} and ℓ_D are assumed to take the same values for all experimental acquisitions at the various temperatures, while the correlation length ξ is specific to each temperature and the corresponding values are determined from the best fit to the experimental data. Adjusting these fitting parameters of the theoretical potential, it is possible to match the experimental distribution $P_{eq}(r)$ at $t = 0$. By doing so, we have obtained the correlation length ξ of the order parameter fluctuations for each value of the temperature set at the objective,[9] the constant parameters $\ell_D \simeq 13$ nm and $\rho_{es} \simeq 95$ nm, which are in line with the values found in previous investigations.[9,20] As anticipated in Section 2, the actual temperature T of the sample is expected to be a linear combination of the temperature T_{Obj} set at the microscope objective, which is varied during the experiment, and the fixed temperature $T_{ST} = 304.65$ K of the sample stage, *i.e.*,

$$T = (1 - \alpha)T_{ST} + \alpha T_{Obj} \quad (5)$$

with $0 < \alpha < 1$. Furthermore, the theoretically expected temperature dependence of ξ can be expressed as[9]

$$\xi(T) = \xi_0 \left(1 - \frac{T}{T_c}\right)^{-\nu}, \quad (6)$$

where the non-universal length $\xi_0 = 0.20 \pm 0.02$ nm has been determined by light-scattering experiments for the water-2,6-lutidine mixture,[31] and $\nu = 0.63$ is a universal bulk critical exponent for the Ising universality class valid for classical binary liquid mixtures.[20] Eqn (5) and (6) can be combined in

Table 1 First column: values of the bulk correlation length ξ as explored in the present experiment and obtained from the best fit to the experimental distribution $P_{eq}(r)$, corresponding to various sample temperatures, which are reported in the second column. In the third column, the corresponding values of $\Delta T = T_c - T$ are reported, with $T_c = 307.01 \pm 0.17$ K

ξ (nm)	T (K)	ΔT (mK)
10	306.55	0.456
18	306.74	0.273
22	306.81	0.200
24	306.85	0.163
30	306.88	0.127
32	306.90	0.108

order to fit the experimental values of ξ, obtained before and corresponding to the various experimentally set and controlled temperatures T_{Obj}, using T_{Obj}, T_{ST}, ξ_0, and ν as input parameters with α and T_c as fitting parameters. In particular, we obtained $T_c = 307.01 \pm 0.17$ K and $\alpha = 0.367 \pm 0.074$. This value of α was used, according to eqn (5), in order to calculate the actual sample temperature corresponding to each value of ξ reported in Table 1.

Once these parameters are fixed to their best-fit values, the resulting total potential $V_{es} + V_C$, reported in Fig. 5 for the values of the parameters relevant for the current experiment, is used to simulate the ensuing evolution by Brownian dynamics, taking into account the distribution of the initial conditions. The core of a Brownian dynamics simulation is given by the Langevin equation, which is a stochastic differential equation describing the time evolution of a particle performing Brownian motion. It is integrated in time in order to create trajectories of the particle.[32]

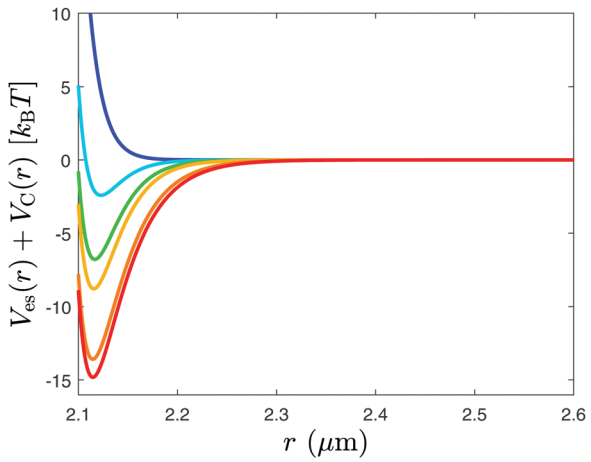

Fig. 5 Total potential in the absence of the optical tweezers, resulting from the electrostatic and critical Casimir forces acting on the particles for various values of the correlation length $\xi = 10$ nm (blue), 18 nm (light blue), 22 nm (green), 24 nm (yellow), 30 nm (orange), and 32 nm (red), where all the other relevant parameters (such as $\rho_{es} \simeq 95$ nm and $\ell_D \simeq 13$ nm) have been fixed at their best-fit values. Upon increasing the correlation length (*i.e.*, upon approaching T_c), the total potential is reduced compared to its value far from criticality, and it assumes negative values within those ranges of distances, where the particles tend to be confined. When the interparticle distance is larger than *ca.* 2.3 μm, the total potential (and therefore the force) practically vanishes for all values of the correlation length explored in the present experiment.

We emphasise that, while the optical tweezers are switched off, *i.e.*, with $V_{ot,l} = 0$, the particles undergo Brownian motion and diffuse under the influence of the CCFs (due to V_C) and of the electrostatic interaction (due to V_{es}).

3.3 Diffusion and drift velocity

The relative position and the distance between the two particles can be used to determine the values of their diffusion constant $D(r)$ and of their drift velocity $v(r)$ as functions of r.[33] Given the experimental trajectories of the particles as a sequence of values r_i, numbered by i and acquired at times $i \times t_s$, where t_s is the time between sampling, one has

$$D(r) = \frac{1}{2}\left\langle \frac{(r_{i+n} - r_i)^2}{nt_s} \middle| r_i \in [r - \delta r, r + \delta r] \right\rangle \quad (7)$$

and

$$v(r) = \left\langle \frac{r_{i+n} - r_i}{nt_s} \middle| r_i \in [r - \delta r, r + \delta r] \right\rangle, \quad (8)$$

where $\langle \ldots | \ldots \rangle$ denotes the average over the various trajectories under the specified condition; $\delta r = 10$ nm is the spatial resolution for $D(r)$ and $v(r)$, with $n = 3$ for determining the diffusion coefficient and $n = 10$ for the drift. These values of n have been chosen separately as the smallest integers which render statistically meaningful, almost n-independent values for $D(r)$ and $v(r)$. In particular, in order to estimate the actual diffusion coefficient *via* the estimator D, it would be desirable to consider small values of n in such a way that the potential effects of a deterministic drift are negligible (see also the discussion below). On the contrary, for the calculation of v, it would be preferable to consider larger values of n, in order for the effects of diffusion to average out. However, exceedingly small values of n yield numerical data for D with large statistical fluctuations, while exceedingly large values of n would not allow for a proper identification of the spatial dependence of $v(r)$. The choices indicated above emerge from a compromise between these competing requests. In eqn (7) [and in, *cf*, eqn (11) and (12)], the actual diffusion constant is determined from the experimental data *via* the estimator $D = \langle(\Delta r)^2\rangle/(2\Delta t)$, in terms of the (conditional) average of the displacement Δr observed within a suitable time interval Δt (= nt_s in eqn (7)). However, an alternative estimator for the same quantity is $\hat{D} = [\langle(\Delta r)^2\rangle - \langle\Delta r\rangle^2]/(2\Delta t)$, which is closer to the common definition of the diffusion constant and which highlights the sole effect of the Brownian noise, as it subtracts a possible mean drift $\langle\Delta r\rangle$ of the particles due to the action of external forces in the presence of overdamped dynamics. These two estimators are actually related by $\hat{D} = D - \Delta t v^2/2 + \mathcal{O}((\Delta t)^2)$, where $v = \langle\Delta r\rangle/\Delta t$ is the average relative velocity of the particles, and therefore they render the same value for sufficiently small Δt or whenever v vanishes due to the absence of external forces. In the present experiment, we considered the estimator D instead of $\hat{D}$ for three reasons: (a) Since $\langle\Delta r\rangle$, *i.e.*, $v\Delta t$ is affected by statistical errors, subtracting it from $\langle(\Delta r)^2\rangle$ increases the resulting statistical error of $\hat{D}$ compared to

that of D; (b) at distances r larger than *ca.* 2.2 μm, we expect all deterministic forces involved to vanish in the absence of the tweezers and therefore $v = 0$, such that $D = \hat{D}$; (c) at smaller distances, but for sufficiently small values of Δt, *i.e.*, for $\Delta t \ll D/v^2$, the two estimators $\hat{D}$ and D are anyhow approximately equal. Both estimators $D(r)$ and $\hat{D}(r)$ render the actual diffusion coefficient as $\Delta t \to 0$ but they are generically affected by (different) finite-time corrections which depend on r, are linear in Δt for small Δt, and are related as discussed above.†

Due to the hydrodynamic interaction between the two colloids, the actual diffusion constant of these particles differs from the free one they would have in the bulk.[34] As a result, the diffusion along the direction connecting the centers of the particles occurs with a diffusion constant which differs from that in the direction perpendicular to it (see eqn (5.5) in ref. 34). In order to compare our experimental results with these theoretical predictions, we decompose the ith displacement $\Delta\mathbf{r}_i^{(n)} = \mathbf{r}_{i+n} - \mathbf{r}_i$ into its parallel and perpendicular components:

$$\Delta r_{i\parallel}^{(n)} = \Delta\mathbf{r}_i^{(n)}\cdot\hat{\mathbf{r}}_i \tag{9}$$

and

$$\Delta r_{i\perp}^{(n)} = \Delta\mathbf{r}_i^{(n)}\cdot(\hat{\mathbf{z}}\times\hat{\mathbf{r}}_i), \tag{10}$$

where $\hat{\mathbf{r}}_i = \mathbf{r}_i/r_i$ and $\hat{\mathbf{z}}$ is the unit vector along the z-direction, which is perpendicular to the xy-plane of observation where the position vectors $\mathbf{r}_i$ lie. With these definitions, we can obtain the parallel and perpendicular diffusion coefficients defined with respect to the direction connecting the centers of the two particles:

$$D_\parallel(r) = \frac{1}{2}\left\langle \frac{\left|\Delta r_{i\parallel}^{(n=3)}\right|^2}{3\times t_s}\,\middle|\, r_i\in[r-\delta r, r+\delta r]\right\rangle, \tag{11}$$

and

$$D_\perp(r) = \frac{1}{2}\left\langle \frac{\left|\Delta r_{i\perp}^{(n=3)}\right|^2}{3\times t_s}\,\middle|\, r_i\in[r-\delta r, r+\delta r]\right\rangle, \tag{12}$$

† In order to illustrate the emergence of these corrections *via* using a simple example, we assume that the dynamics of the distance r under the sole effect of the interparticle potential $V_{es} + V_C$ is described by the overdamped Langevin equation $\dot{r} = f(r) + \sqrt{2\mathscr{D}(r)}\eta(t)$, where $f(r)$ is proportional to the deterministic forces acting on the particles (due to that potential), $\eta(t)$ is a Gaussian noise with $\langle\eta(t)\rangle = 0$, and $\langle\eta(t)\eta(t')\rangle = \delta(t-t')$, while $\mathscr{D}(r) > 0$ is the position-dependent diffusion constant. This stochastic differential equation is interpreted according to the Îto convention, while here we neglect the fact that r is actually the projection of the interparticle distance onto the xy-plane. A relatively simple but lengthy calculation shows that by defining $D(r)$ as in eqn (7), *i.e.*, from the conditional expectation of the increments Δr of the variable r within a time interval of finite duration Δt, one finds $D(r) = \mathscr{D}(r) + (\Delta t/2)c_1(r) + \mathscr{O}((\Delta t)^2)$, where $c_1(r) = f^2(r) + 2\mathscr{D}(r)f'(r) + \mathscr{D}'(r)f(r) + \mathscr{D}(r)\mathscr{D}''(r)$ is the leading finite-time bias of the estimator D of the actual diffusion $\mathscr{D}$. We emphasize that $c_1(r)$ vanishes at large separations because, correspondingly, $f(r)$ generically decays to zero while $\mathscr{D}(r)$ approaches its bulk, r-independent value. In addition, the sign of $c_1(r)$ may change as a function of r. In particular, one has $c_1(r) < 0$ when r approaches a point r_0 of stable mechanical equilibrium [*i.e.*, with $f(r_0) = 0$ and $f'(r_0) < 0$] with $\mathscr{D}''(r_0) < 0$, as in the case of the theoretical diffusion coefficients reported in Fig. 6.

respectively, and the parallel and perpendicular drift velocities:

$$v_\parallel(r) = \left\langle \frac{\Delta r_{i\parallel}^{(n=10)}}{10\times t_s}\,\middle|\, r_i\in[r-\delta r, r+\delta r]\right\rangle, \tag{13}$$

and

$$v_\perp(r) = \left\langle \frac{\Delta r_{i\perp}^{(n=10)}}{10\times t_s}\,\middle|\, r_i\in[r-\delta r, r+\delta r]\right\rangle, \tag{14}$$

respectively. The remark about the use of the estimator D instead of $\hat{D}$, stated after eqn (7), here applies to $D_\parallel$, while $D_\perp$ is not affected by the choice of the estimator because no forces are expected to act along the direction perpendicular to the segment joining the centers of the colloids. In Fig. 6 we report the experimental data (symbols) for $D_\perp$ (upper set) and $D_\parallel$ (lower set) as functions of the ratio r/d, together with the theoretical prediction obtained in ref. 34 (solid line) for no-slip boundary conditions. These quantities are normalized by the bulk inter-particle diffusion constant given by (see, *e.g.*, eqn (5.6) in ref. 34)

$$D_0 = \frac{k_B T}{3\pi\eta d/2} \simeq 0.22\ (\mu m)^2\ s^{-1}, \tag{15}$$

in terms of the viscosity $\eta \simeq 2\times10^{-3}$ Ns m^{-2} of the mixture close to T_c.[35] (The expected singularity of D_0 and η upon approaching criticality is so mild that it can be neglected for

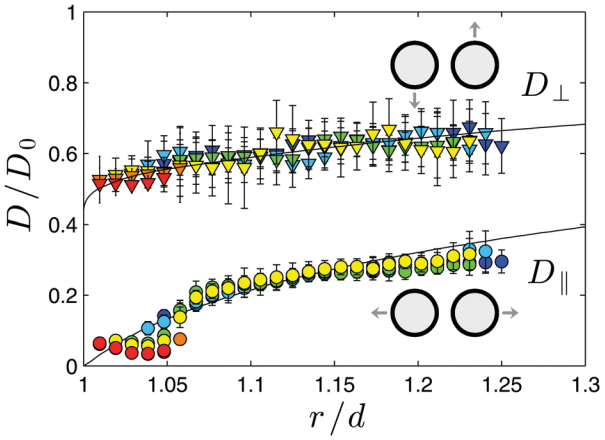

Fig. 6 Experimental values of the normalized parallel $D_\parallel/D_0$ (circles) and perpendicular $D_\perp/D_0$ (triangles) diffusion constants as functions of the ratio between the inter-particle center-to-center distance r and the particle diameter d. The parallel and perpendicular directions refer to the line connecting the centers of the two colloids, and D_0 is the bulk diffusion constant determined by eqn (15) and from available experimental data. The various colors refer to data taken at ΔT = 456 ± 2 mK (blue), 273 ± 2 mK (light blue), 200 ± 2 mK (green), 163 ± 2 mK (yellow), 127 ± 2 mK (orange), and 108 ± 2 mK (red). The solid lines represent the theoretical predictions accounting for the effect of the hydrodynamic interaction between the colloids.[34] Error bars represent the standard deviation of the experimental values. There is good agreement between the theoretical predictions and the experimental results, which neither exhibit an appreciable dependence on temperature. The nature of the deviations observed in $D_\parallel$ at short and long distances is discussed in the main text.

all practical purposes.[36,37]) Both for $D_\perp$ and $D_\parallel$ Fig. 6 shows satisfactory agreement, with a systematic discrepancy emerging only in $D_\parallel$ for $r/d \lesssim 1.05$. This discrepancy is due to the limited experimental acquisition rate, which does not allow us to resolve times shorter than 3 ms. In fact, the same discrepancy is encountered in simulations when we consider trajectories sampled with the same time step t_s as the one used in the experiment. If we reduce significantly the time step t_s in the simulations, the discrepancy with the theoretical line is much less pronounced and eventually disappears, as it is expected from the fact that the latter should be recovered as $t_s \to 0$. Similarly, at large values of r/d, the experimental values of the parallel diffusion $D_\parallel$ coefficient differ from the corresponding theoretical prediction (Fig. 6) because of the finite experimental time during which the data are acquired, *i.e.*, because of the finite size of the sample of data over which the average is calculated. This discrepancy could be reduced by acquiring the experimental data for a longer time. In addition, we note that both in experiment and simulation, values of r/d which are smaller than 1.05 are obtained only when the temperature T is sufficiently close to T_c and, thus, sizable CCFs are present, especially at such short distances. Their presence implies $v \neq 0$ and therefore we expect finite-time corrections to appear in $D_\parallel \simeq \hat{D}_\parallel + v_\parallel{}^2 \Delta t/2$ in addition to those which characterize $\hat{D}_\parallel$. The experimental data for $D_{\perp,\parallel}$ reported in Fig. 6 do not show any significant dependence on ΔT and ξ, apart from the finite-time effects mentioned above. A genuine temperature dependence of $D_{\perp,\parallel}$ could be expected for Brownian particles diffusing near T_c in an external potential, provided by strongly temperature-dependent critical fluctuations which alter the dynamics (see, *e.g.*, ref. 38 and 39 for a single trapped colloid). Accordingly, the absence of this dependence suggests that the effective interaction V_C is valid, for all practical purposes, as if the colloidal particles were at rest in their instantaneous position. In our specific case, in fact, the typical timescale of colloid diffusion is 50 times larger than the relaxation time of critical fluctuations. Similarly, the distortion of the equilibrium order parameter profile around the colloids due to their deterministic motion is negligible, because the Péclet number which quantifies the magnitude of this effect (see ref. 40 for details) turns out to be at most 4×10^{-3}, which is extremely small‡. This also implies that for the present experimental conditions the effects of retardation, observed numerically in ref. 41 during the aggregation of two identical colloids due to CCFs, are negligible.

In the first two columns of Fig. 7, we report the values of the experimental and simulated drift velocities $v_\parallel$ and $v_\perp$ as functions of r/d and for decreasing values of ΔT from top to bottom. The theoretical values of the drift velocities are calculated by employing eqn (13) and (14) for the simulated trajectories. These trajectories are obtained from Brownian dynamics simulations of two particles interacting *via* the total potential $V = V_C + V_{es}$. We simulate a Langevin equation along the lines of ref. 32, with the diffusion coefficients $D_{\perp,\parallel}$ following from eqn (5.5) and Fig. 3 in ref. 34 (see also Fig. 6 here) and based on the value of D_0 as given by eqn (15). The parameters ξ, ℓ_D, and ρ_{es} are fixed to their best-fit values obtained by fitting the initial distribution $P_{eq}(r)$ as described above [see eqn (4) and (3)].

At large values of ΔT (Fig. 7a and d), the parallel drift velocity $v_\parallel$ is positive at small values of r/d because, on average, the particles are pushed away from each other by the dominating repulsive electrostatic potential V_{es}. Increasing the value of r/d, $v_\parallel$ rapidly vanishes because, correspondingly, the electrostatic repulsion decays exponentially on a scale set by $\ell_D \simeq 13$ nm, corresponding to $\ell_D/d \simeq 6 \times 10^{-3}$ on the scale of the plot. Upon decreasing ΔT, as in Fig. 7g and j, $v_\parallel$ becomes negative within a certain range of values of r/d. At these distances, the particles move on average towards each other due to the attractive critical Casimir interaction V_C, which competes and eventually overcomes the electrostatic interaction V_{es}. However, at smaller values of r/d, V_{es} dominates and $v_\parallel$ is no longer negative. If ΔT is reduced further, $v_\parallel$ becomes quickly more negative (Fig. 7m and p), because the attractive critical Casimir interaction is so strong that it moves the particles towards each other until their velocity vanishes at contact. At larger distances, instead, $v_\parallel$ vanishes and the particles undergo Brownian diffusion. We note that this range of distances can actually be explored only *via* numerical simulations with sufficiently high statistics. In the experiment, instead, the particles turn out to stick almost always together, and they explore the very limited range of distances indicated on the solid horizontal axes.

The experimental and numerical determination of the orthogonal component $v_\perp$ of the drift velocity (eqn (14)) is reported in the second column of Fig. 7. Here, $v_\perp$ vanishes in all the cases investigated because all the forces at play in the present experiment act along the direction which connects the centers of the particles. Accordingly, $v_\perp$ shows no temperature dependence.

The third column of Fig. 7 reports the total force field (resulting from the sum of the electrostatic force and of the attractive CCF) in the xy-plane used in the numerical simulation. The length of the arrows corresponding to each point in that plane is proportional, for the purpose of visualization, to the logarithm of the magnitude of the total force. Blue arrows indicate repulsive forces, whereas red arrows indicate attractive ones.

It is noteworthy that the agreement observed in Fig. 6 and 7 between the experimental and simulated data confirms the reliability of the model we have used.

‡ The typical timescale of a colloidal diffusion process can be estimated by the time t_{coll} the colloid takes to diffuse across a reference distance L (*e.g.*, its radius $d/2$): $t_{coll} = L^2/D_0$, where $D_0 = k_B T/(6\pi\eta d/2)$ is the diffusion constant of a colloid with diameter d in a fluid with dynamic viscosity η. Similarly, according to mode coupling theory,[40] the mutual diffusion constant D_ξ of the order parameter fluctuations is given by $D_\xi = k_B T/(6\pi\eta\xi)$, where ξ is the correlation length of the critical fluctuations, which in the present experiment ranges between 10 and 30 nm (see Table 1). Accordingly, the typical timescale t_ξ of the diffusion of critical fluctuations is $t_\xi = L^2/D_\xi$ and the ratio of these two typical timescales is $t_{coll}/t_\xi = D_\xi/D_0 \simeq 50$, as reported in the main text. Similarly, the deterministic motion of the colloid may cause a distortion of the order parameter profile around the colloids, which was investigated in ref. 40. The magnitude of this effect turns out to be quantified by the Péclet number[40] $\mathrm{Pe} = \xi|v_0|/D_\xi$, where v_0 is the typical velocity of the motion, which, in the present experiment (see Fig. 7), takes a maximal value of approximately 0.5 μm s^{-1}. Accordingly, the maximum value of Pe turns out to be approximately 4×10^{-3}, which is an extremely small value.

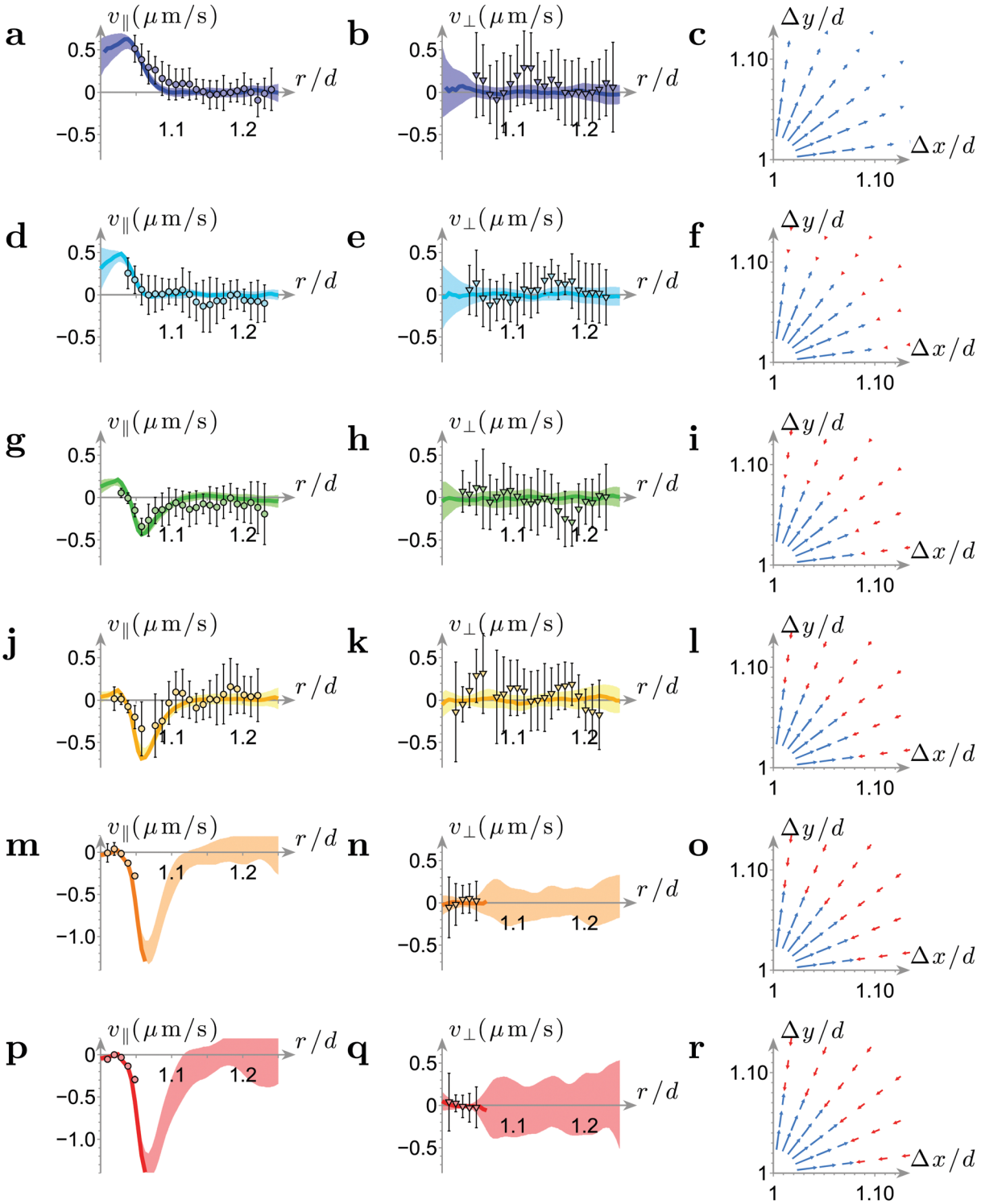

Fig. 7 The drift velocities $v_\parallel$ (first column) and $v_\perp$ (second column), parallel and perpendicular, respectively, to the direction connecting the centers of the two colloids and the total force field (in arbitrary units) used as the basis of the simulations (third column) are represented for (a–c) $\Delta T = 456 \pm 2$ mK, (d–f) 273 ± 2 mK, (g–i) 200 ± 2 mK, (j–l) 163 ± 2 mK, (m–o) 127 ± 2 mK, and (p–r) 108 ± 2 mK. In the first two columns, the symbols with error bars represent the experimental data, and the thick, colored lines represent the corresponding simulation results. The shaded areas represent the error of the numerical estimates due to the uncertainties in the fit parameters. In order to visualize the total force field F resulting from the electrostatic repulsion and the CCFs (*i.e.*, from the potential $V_{es} + V_C$), in the third column we plot within the Δx–Δy plane ($\Delta x = x_2 - x_1$ and $\Delta y = y_2 - y_1$) the corresponding vector, indicating repulsion by blue arrows and attraction by red ones. Their length corresponds to $4.6 \times 10^{-3} \log_{10}(|F|/10fN)$ for the scale used.

3.4 First passage times

In order to highlight the effect of CCFs on the dynamics of the two colloidal particles, we consider the first-passage time t_1, *i.e.*, the time it takes that the particles reach for the first time a reference separation r_{ref}, starting from a certain initial distance r_{in}. Heuristically, this quantity provides a measure of how much the interaction effectively speeds up or slows down the relative diffusion process of the two particles, t_1 being the minimal time required by the colloids to realize a certain configuration.

The first-passage time is a random variable which changes for each realization of the diffusion process. Accordingly, it can be characterized by its cumulative probability distribution $P_1(t)$ that t_1 is smaller than a given time t, which depends on the choice of r_{in} and r_{ref}. (In order to smooth out statistical fluctuations of the experimental data, it is convenient here to focus on the cumulative distribution of t_1 instead of its probability distribution $p(t_1)$, which can in principle be obtained as $p(t_1) = (\mathrm{d}P_1(t)/\mathrm{d}t)|_{t=t_1}$.) In order to determine P_1, for each value of ΔT and each repetition of the blinking process, in which the particles are initially separated by a distance r_{in}, we measure the time t_1 it takes them to reach the separation r_{ref} for the first time, while the optical traps are turned off. Based on these data, $P_1(t)$ at a certain time t is determined by the ratio between the number of occurrences for which $t_1 < t$ and the total number of collected data. The experimental results are presented in Fig. 8a and b for $r_{in} = 2.16\ \mu m < r_{ref}$ and $r_{in} = 2.40\ \mu m > r_{ref}$, respectively, with $r_{ref} = 2.22\ \mu m$ in all cases.

First, we consider the case of the first passage time from $r_{in} = 2.16\ \mu m$ to $r_{ref} = 2.22\ \mu m$, as shown in Fig. 8a. Far from criticality ($\Delta T = 456 \pm 2$ mK), the repulsive electrostatic interaction (see Fig. 5 for the corresponding potentials) dominates for $r < r_{ref}$ and therefore, as the particles are pushed away from each other, $P_1(t)$ rapidly reaches its maximal value 1. However, upon approaching criticality, the increasingly strong, attractive critical Casimir interaction, acting for $r < r_{ref}$, effectively slows down the separation of the particles, so that $P_1(t)$ approaches its maximum value 1 only at long times.

Setting the initial condition outside the range of action of the CCFs, *i.e.*, for $r_{in} = 2.40\ \mu m$, $P_1(t)$ has a significantly less pronounced dependence on ΔT, at least within the range of parameters explored here (Fig. 8b). This is due to the fact that the temperature dependent CCFs are actually negligible for $r > r_{ref}$. In particular, the total potential does not change as a

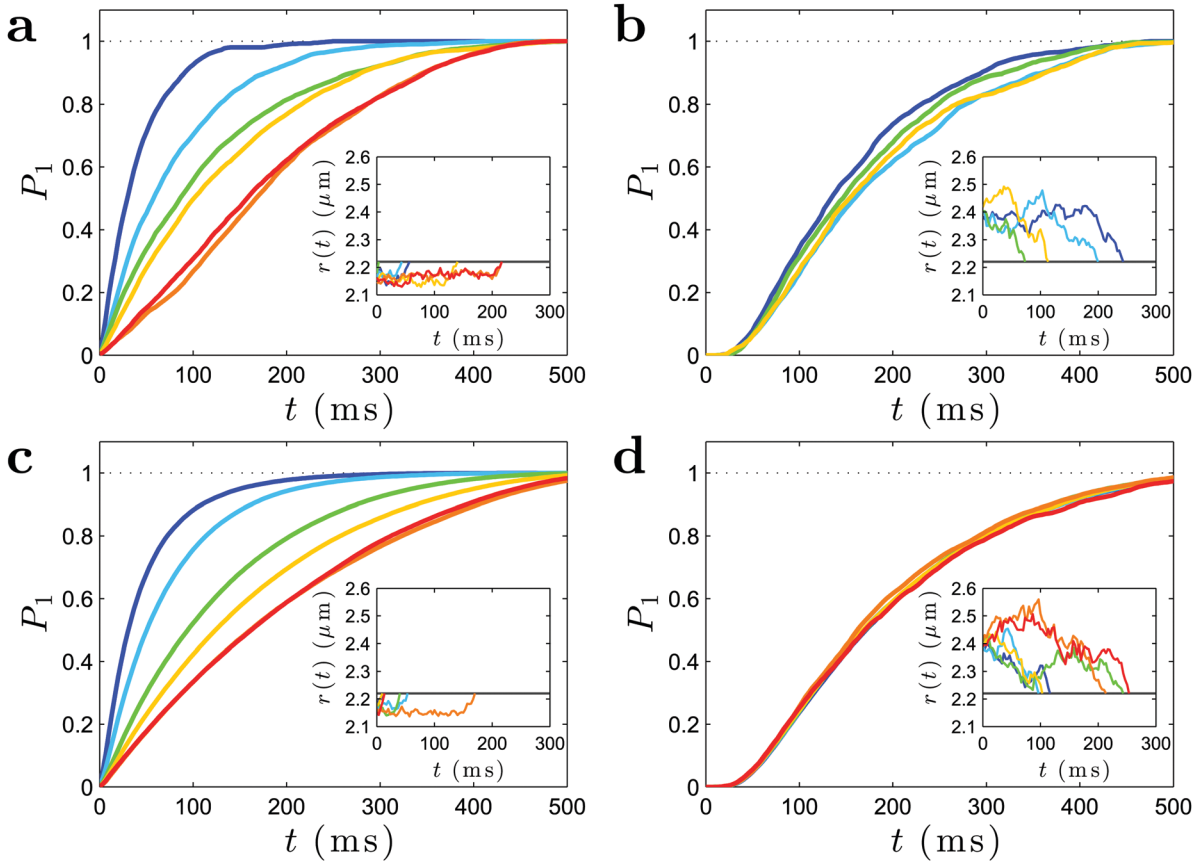

Fig. 8 Cumulative probability $P_1(t)$ of first-passage times at a certain inter-particle distance as a function of time for various temperatures. (a and b) Experimentally and (c and d) numerically determined probability distribution $P_1(t)$ to reach the reference distance $r_{ref} = 2.22\ \mu m$ for the first time earlier than a given time t, when the particles start from an initial distance (a and c) $r_{in} = 2.16\ \mu m < r_{ref}$ and (b and d) $r_{in} = 2.40\ \mu m > r_{ref}$. The lines of various colors refer to $\Delta T = 456 \pm 2$ mK (blue), 0.2730 ± 2 mK (light blue), 200 ± 2 mK (green), 163 ± 2 mK (yellow), 127 ± 2 mK (orange), and 108 ± 2 mK (red). The insets in the various panels show, on the same scale, representative trajectories of $r(t)$ for various temperatures (the horizontal solid lines correspond to r_{ref}). In panel (d) and on that scale, the various curves are almost indistinguishable.

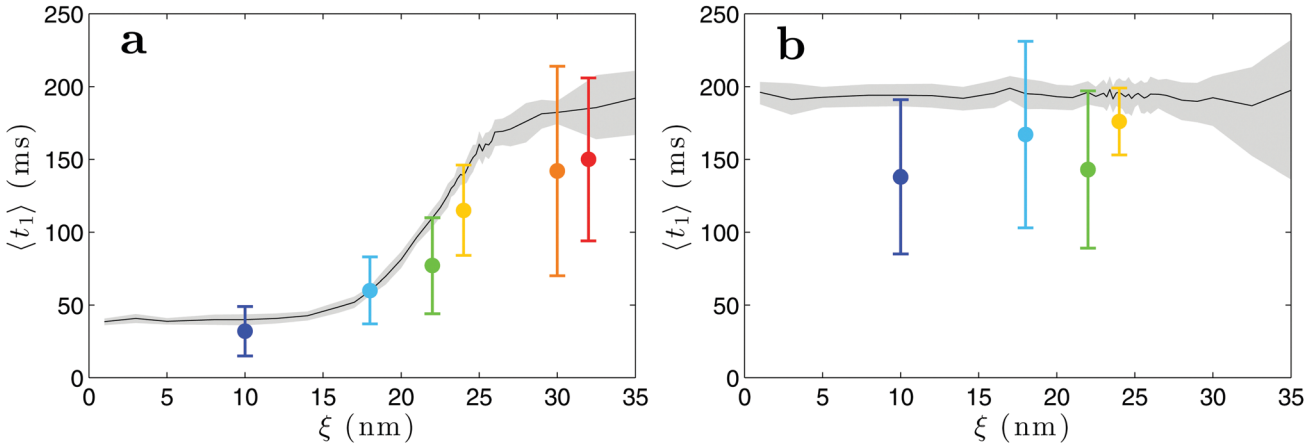

Fig. 9 Mean first-passage time $\langle t_1 \rangle$, as a function of the correlation length ξ, to reach for the first time the reference distance r_{ref} = 2.22 μm from the initial distance (a) r_{in} = 2.16 μm and (b) 2.40 μm. Symbols with error bars represent the experimental data while black solid lines with greyly shaded area correspond to simulation data and their uncertainties. The color code for the temperatures is the same as the one used in Fig. 6 and 7. Here, $\langle t_1 \rangle$ is reported as a function of the associate correlation lengths ξ instead of ΔT; specifically, ξ = 10 nm (blue), 18 nm (light blue), 22 nm (green), 24 nm (yellow), 30 nm (orange), and 32 nm (red).

function of temperature, because this range of distances is anyhow much larger than that of the correlation length of the critical fluctuations explored in the present experiment. In fact, a behavior similar to that reported in Fig. 8a can be observed for $r > r_{ref}$ only for values of the correlation length ξ significantly larger than those achieved here.

The results of corresponding Langevin-dynamics simulations are presented in Fig. 8c and d. These simulations are in very good agreement with the experimental data presented in Fig. 8a and b, respectively. This agreement further validates our simulation model, which is based on an interaction potential $V(\rho) = V_C(\rho) + V_{es}(\rho)$, as a function of the surface-to-surface distance ρ between the particles, with a diffusion term described according to eqn (11) and (12).[9]

The results reported in Fig. 8 can be made more quantitative by calculating the mean first-passage time $\langle t_1 \rangle = \int_0^{+\infty} dt_1 t_1 p(t_1) = \int_0^{+\infty} dt [1 - P_1(t)]$, which is reported in Fig. 9 as a function of the correlation length ξ corresponding to the values of ΔT used in Fig. 8. For r_{in} = 2.16 μm and r_{ref} = 2.22 μm (Fig. 8a and c), $\langle t_1 \rangle$ increases upon increasing the correlation length ξ (Fig. 9a), because the attractive interaction due to V_C slows down the diffusion of the particles. Instead, for r_{in} = 2.40 μm and r_{ref} = 2.22 μm (Fig. 8b and d), no significant dependence of $\langle t_1 \rangle$ on ξ is observed (Fig. 9b), because the CCFs are negligible for $r \gtrsim r_{ref}$ within the range of values of ξ explored here.

4 Conclusions

We have shown that by using blinking optical tweezers it is possible to investigate the dynamics of a pair of colloidal particles, dispersed in a critical, binary liquid solution of water and 2,6-lutidine, in the absence of optical potentials and, thus, occurring under the influence of their effective inter-particle interaction only. Digital video microscopy facilitated to track the positions of the particles and to determine the effects of the CCFs on the time evolution of their center-to-center distance r upon approaching the critical temperature of the solvent. In order to infer the correlation length ξ of the critical fluctuations and the strength of the corresponding CCF, we have compared the experimental data for the equilibrium distribution of the inter-particle distance in the presence of optical traps with the results of a Monte Carlo integration of the expected Boltzmann distribution. The resulting fitted parameters have been used to perform a simulation of the dynamics of the two interacting colloids immersed in the same solvent. The very good agreement between the experimental data and the corresponding numerical simulations based on Langevin dynamics has validated the theoretical description of the forces involved and of the dynamics, which does not require accounting for the possible effects of retardation.[41] This holds at least within the range of parameters explored here. The agreement between theory and experiment has also provided information about the correlation length ξ of the critical fluctuations and about the CCF field, for various temperatures approaching the critical point. Moreover, the knowledge of the first passage time relative to a start and a final configuration, in which the particles are essentially fully separated, is crucial for understanding the dynamics and to eventually control the self-assembly process of many colloidal particles. In particular, the model used here can be exploited to create a base protocol for the application and for the fine tuning of CCFs towards their use for nanotechnology. This offers new possibilities for the design and realization of self-assembled nano-structures and for driving nano-devices.

Conflicts of interest

There are no conflicts to declare.

Acknowledgements

This work was partially supported by the ERC Starting Grant ComplexSwimmers (grant no. 677511) and by Vetenskapsrådet (grant no. 2016-03523). A. C. acknowledges partial financial support from TUBITAK (grant no. 116F111). J. P. S. acknowledges partial financial support from FONDECYT (grant no. 117103).

Notes and references

1 M. E. Fisher and P. G. de Gennes, *C. R. Acad. Sci., Paris*, 1978, **287**, 207.
2 M. Krech, *Casimir Effect in Critical Systems*, World Scientific, Singapore, 1994.
3 G. Brankov, N. S. Tonchev and D. M. Danchev, *Theory of Critical Phenomena in Finite-Size Systems*, World Scientific, Singapore, 2000.
4 A. Gambassi, *J. Phys.: Conf. Ser.*, 2009, **161**, 012037.
5 A. Gambassi and S. Dietrich, *Soft Matter*, 2011, **7**, 1247.
6 H. B. G. Casimir, *Proc. K. Ned. Akad. Wet.*, 1948, **51**, 793.
7 C. Hertlein, L. Helden, A. Gambassi, S. Dietrich and C. Bechinger, *Nature*, 2008, **451**, 172.
8 F. Soyka, O. Zvyagolskaya, C. Hertlein, L. Helden and C. Bechinger, *Phys. Rev. Lett.*, 2008, **101**, 208301.
9 S. Paladugu, A. Callegari, Y. Tuna, L. Barth, S. Dietrich, A. Gambassi and G. Volpe, *Nat. Commun.*, 2016, **7**, 11403.
10 D. Bonn, J. Otwinowski, S. Sacanna, H. Guo, G. Wegdam and P. Schall, *Phys. Rev. Lett.*, 2009, **103**, 156101.
11 A. Gambassi and S. Dietrich, *Phys. Rev. Lett.*, 2010, **105**, 059601.
12 R. Piazza, S. Buzzaccaro, A. Parola and J. Colombo, *J. Phys.: Condens. Matter*, 2011, **23**, 194114.
13 E. Marino, T. E. Kodger, J. B. ten Hove, A. H. Velders and P. Schall, *Sol. Energy Mater. Sol. Cells*, 2016, **158**, 154.
14 T. A. Nguyen, A. Newton, D. J. Kraft, P. G. Bolhuis and P. Schall, *Materials*, 2017, **10**, 1265.
15 F. Schmidt, A. Magazzù, A. Callegari, L. Biancofiore, F. Cichos and G. Volpe, *Phys. Rev. Lett.*, 2018, **120**, 068004.
16 U. Nellen, L. Helden and C. Bechinger, *Europhys. Lett.*, 2009, **88**, 26001.
17 M. Tröndle, O. Zvyagolskaya, A. Gambassi, D. Vogt, L. Harnau, C. Bechinger and S. Dietrich, *Mol. Phys.*, 2011, **109**, 1169.
18 I. A. Martnez, C. Devailly, A. Petrosyan and S. Ciliberto, *Entropy*, 2017, **19**, 77.
19 C. A. Grattoni, R. A. Dawe, C. Y. Seah and J. D. Gray, *J. Chem. Eng. Data*, 1993, **38**, 516.
20 A. Gambassi, A. Maciołek, C. Hertlein, U. Nellen, L. Helden, C. Bechinger and S. Dietrich, *Phys. Rev. E*, 2009, **80**, 061143.
21 D. G. Grier, *Nature*, 2003, **424**, 810.
22 P. H. Jones, G. Volpe and O. Maragò, *Optical Tweezers: Principles and Applications*, Cambridge University Press, 2015.
23 D. G. Grier, *Curr. Opin. Colloid Interface Sci.*, 1997, **2**, 264.
24 G. Pesce, G. Rusciano and A. Sasso, *Opt. Express*, 2010, **18**, 2116.
25 G. Pesce, G. Volpe, G. Volpe and A. Sasso, *Phys. Rev. E*, 2014, **90**, 042309.
26 J. C. Crocker and D. G. Grier, *J. Colloid Interface Sci.*, 1996, **179**, 298.
27 J. Baumgartl and C. Bechinger, *Europhys. Lett.*, 2005, **71**, 487.
28 O. Vasilyev, A. Gambassi, A. Maciołek and S. Dietrich, *EPL*, 2007, **80**, 60009.
29 O. Vasilyev, A. Gambassi, A. Maciołek and S. Dietrich, *Phys. Rev. E*, 2009, **79**, 041142.
30 M. Hasenbusch, *Phys. Rev. B*, 2012, **85**, 174421.
31 E. Gülari, A. F. Collings, R. L. Schmidt and C. J. Pings, *J. Chem. Phys.*, 1972, **56**, 6169.
32 G. Volpe and G. Volpe, *Am. J. Phys.*, 2013, **81**, 224.
33 T. Brettschneider, G. Volpe, L. Helden, J. Wehr and C. Bechinger, *Phys. Rev. E*, 2011, **83**, 041113.
34 G. K. Batchelor, *J. Fluid Mech.*, 1976, **74**, 1.
35 J. C. Clunie and J. K. Baird, *Phys. Chem. Liq.*, 1999, **37**, 357.
36 A. Stein, S. J. Davidson, J. C. Allegra and G. F. Allen, *J. Chem. Phys.*, 1972, **56**, 6164.
37 J. C. Nieuwoudt and J. V. Sengers, *J. Chem. Phys.*, 1989, **90**, 457.
38 Y. Fujitani, *J. Phys. Soc. Jpn.*, 2017, **86**, 114602.
39 Y. Fujitani, *J. Phys. Soc. Jpn.*, 2016, **85**, 044401.
40 A. Onuki, *Phase transition dynamics*, Cambridge University Press, 2002.
41 A. Furukawa, A. Gambassi, S. Dietrich and H. Tanaka, *Phys. Rev. Lett.*, 2013, **111**, 055701.